Nano Research

Open Access

Research Article

Intrinsic fiber reinforced polyimide aerogel flexible strain sensor applied in high-temperature environment

Jinming Liu[1], Ling Weng[1,2] ✉, Xiaorui Zhang[1], Xiaoming Wang[1], and Zijian Wu[1]

[1] *School of Material Science and Chemical Engineering, Harbin University of Science and Technology, Harbin 150080, China*
[2] *Key Laboratory of Engineering Dielectrics and Application Ministry of Education, Harbin University of Science and Technology, Harbin 150080, China*

Cite this article: *Nano Research*, **2025**, *18*, 94907302. https://doi.org/10.26599/NR.2025.94907302

ABSTRACT: Flexible strain sensors have garnered significant attention for their potential applications in advanced flexible electronics and wearable technologies. However, achieving stable signal transmission at high temperatures remains a major challenge. In this study, we developed a novel polyimide (PI) aerogel composite, reinforced with intrinsically short-cut polyimide nanofibers (PINF) that are surface-coated with silver nanoparticles to enhance both conductivity and mechanical strength. Carbon nanotubes (CNTs) are used as the main filler in synergistic effect with Ag@PINF particles to further improve the conductivity and sensing performance of the composite material. This synergistic design results in a flexible PI aerogel composite material with rapid response time (116 ms), high sensitivity (GF = 3.12), and long-term cycling stability (> 1000 cycles). Additionally, the sensing materials were tested at high temperatures and after high-temperature aging, demonstrating good flexible sensing performance. Experimental results demonstrate that the composite sensor maintains stable strain-sensing performance across a range of environmental temperatures, showing consistent strain response under the same deformation conditions. This work provides a promising approach for fabricating high-performance, temperature-resistant flexible strain sensors, with broad applications in flexible electronics and wearable technologies.

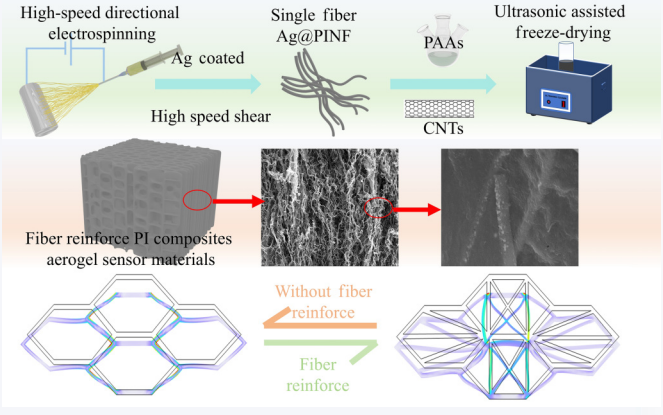

KEYWORDS: flexible strain sensors, polyimide aerogel composite, polyimide nanofiber, sensing performance

1 Introduction

Flexible sensors have garnered significant attention due to their unique structural advantages, including ease of processing, good conformability, and low cost. Based on the signal detection method, these sensors can be classified into piezoresistive, capacitive, and piezoelectric types [1–5]. Among these, piezoresistive flexible sensors have attracted the most interest due to their simpler structure, high stability, and straightforward, visible operating mechanism [6, 7]. These attributes result in lower manufacturing costs and make the sensors easier to repair and replace [8]. With the increasing adoption of flexible sensors globally, there has been growing recognition of their potential in extreme environments, such as those involving very high or low temperatures [9].

There are two key considerations in preparing piezoresistive flexible sensors: the selection of matrix resin and conductive filler. Traditional flexible sensing matrix materials, including polyurethane (TPU) [10–13], polydimethylsiloxane (PDMS) [14–19], and ecoflex [20], exhibit inadequate thermal stability, thereby constraining their suitability for applications requiring reliable performance under complex temperature conditions. As scholars gradually deepen their research on flexible sensing materials, professional researchers will also implement the application of flexible strain sensing materials through practical applications from multiple angles. Dong et al. have developed an AI-assisted, wireless, flexible and wearable mechanical luminescent strain sensor system that combines AI with the application of materials [19]. Yang et al. combined the detection of sensor signals with human motion detection through machine learning [17]. Chen and Hang et al. used the porous effect in flexible materials to

Received: January 2, 2025; **Revised:** January 8, 2025
Accepted: February 12, 2025

✉Address correspondence to l.weng@hrbust.edu.cn

prepare flexible sensing materials with multifunctional functions of wave absorption and sensing [21, 22]. By feeding back different electrical signals of finger behavior, Hang used flexible composite sensor materials to achieve encrypted transmission of information in Morse code [23]. Through the research of many scholars, it can be found that piezoresistive flexible sensing materials have good application effects and wide application fields, which have very important research significance. However, common flexible composite materials are usually used in testing environments at room temperature and are not suitable for extreme environments. In addition, the glass transition temperature (T_g) of most elastomers is low, which will lead to performance degradation under high temperature conditions. Therefore, it is essential to explore materials with high-temperature stability [24–27]. Equally important is the selection of conductive fillers, as they determine the stability and sensitivity of the sensor [28–31].

The primary challenge is to optimize the conductive pathway and ensure effective dispersion of the filler. In our previous study [32], we identified polyimide (PI) aerogel as the most promising choice for matrix resin. Adding an appropriate amount of carbon nanotubes (CNTs) enhances the composite aerogel's flexible sensing capabilities, allowing it to withstand extreme environments [18]. However, its inherent defects, such as a high shrinkage rate and significant residual strain during cyclic loading, have severely limited its development [33–36].

Inspired by the structure of insect wings, a natural material with filler-enhanced intrinsic properties can withstand aerodynamic stresses during flight while maintaining high flexibility [37–40]. Similarly, fiber-reinforced composite materials are created by incorporating fibers into polyimide aerogel to strengthen polyimide aerogel sheets. Due to their compatible dispersion characteristics, polyimide fibers are effective as reinforcement materials, resolving the dispersion issues in the aerogel sheets [41, 42]. While the structural enhancement problem has been addressed, the internal conductivity of the composite material remains a challenge. Based on our previous research, the material's overall performance is optimized when 25 wt.% CNTs are incorporated into the composite aerogel [32]. To improve conductivity after adding polyimide nanofibers, functional modification is applied to the surface of the polyimide nanofibers (PINF) to enhance the conductivity of the matrix resin, with silver (Ag) particles loaded onto the surface. During the preparation of polyimide fibers, S–S bonds are introduced to leverage the coordination effect of Ag–S, enabling the *in-situ* growth of silver on the fibers [43]. This process generates new electron transmission sites within the conductive pathway structure of the composite, contributing to the overall structural stability and significantly improving the sensing performance.

Hence, we present a feasible and efficient approach utilizing a unique structure—a flexible strain sensor reinforced with intrinsic polyimide nanofibers and a soft, yet strong, polyimide aerogel matrix. The synergistic incorporation of Ag@PINF and CNTs improves the overall sensing performance. The study introduces an optimized ultrasonic-assisted freeze-drying process, enabling the uniform dispersion of the conductive fillers and improving the aerogel's performance. This structure enables sensing under low pressures, offers high structural stability, and maintains stable performance in high-temperature environments. The fiber-reinforced aerogel exhibits excellent sensitivity (GF = 3.12), ideal response stability (> 1000 cycles), and stable sensing capabilities at elevated temperatures, along with superior mechanical properties. As a novel fiber-reinforced aerogel design, it significantly expands the potential applications of flexible sensing materials in high-temperature environments.

2 Experimental section

2.1 Materials

MWCNTs-COOH(CNTs) were purchased from CarbonFeng Graphene Technology Inc, Suzhou, China. Cellulose nanofibers (CNF) were purchased from QIHONG Inc., Guilin, China. N-Methyl-2-pyrrolidone (NMP), 4,4'-biphthalic anhydride (BPDA), 4,4'-diaminodiphenyl ether (ODA), 4-aminophenyl disulfide (AFD), silver nitrate, absolute ethanol, citric acid, ascorbic acid, and potassium iodide were all purchased from Macklin (Shanghai, China).

2.2 Preparation of Ag@PINF

BPDA, ODA, and AFD were weighed in a molar ratio of 1:0.95:0.05. AFD and ODA were dissolved in NMP and stirred until fully dissolved. BPDA was then added to the solution in batches. After stirring for 5 h, a uniform yellow glue solution was obtained. The solution was transferred into a syringe and placed on a directional spinning machine. A positive voltage of 15 kV was applied to the extrusion section, and a negative voltage of −3.5 kV was applied to the high-speed receiving roller. Following spinning, the fiber was demolded and placed in a 120 °C oven for 1 h to yield high-speed directional spinning fibers. The spun fibers were cut into small pieces and placed in a mixed solution of tert-butylalcohol and water. The fibers were sheared into short-cut fibers using a homogenizer (1.2 krpm/min), and the short-cut fibers were obtained after freeze-drying. The chopped fibers were then placed in an oxygen plasma processor for 5 min of bombardment. PINF was added to a three-necked flask, followed by the addition of deionized water. The oil bath was set to 110 °C, and ascorbic acid was introduced to the boiling water. Within 5 min, a mixed solution of sodium citrate, potassium iodide, and silver nitrate was added, and the reaction continued for 1 h. Ag@PINF chopped fibers were obtained after freeze-drying.

2.3 Preparation of Ag@PINF/CNTs/PI aerogels

The preparation method for polyamic acid salt has been described in detail in our previous study. To prepare the composite, 50 mg of polyamic acid salt (PAAs) was combined with 15 μL of triethylamine (TEA) and 10 mL of deionized water. A solution of 10 mL of CNF-coated CNTs nanopowder (with CNTs content at 25% of the PAAs mass) was added, followed by Ag@PINF chopped fibers according to a predetermined mass ratio. The mixture was subjected to ultrasonic stirring for 20 min, after which it was poured into a mold. The mold was placed in liquid nitrogen to cool anhydrous ethanol to −20 °C, then transferred to an ultrasonic cleaner. The mold was positioned in the cleaner for pre-freezing with the assistance of ultrasound. Following ultrasonic-assisted freezing, the mold was placed in a freeze dryer and freeze-dried for 72 h. The aerogel prepared by ultrasonic-assisted freeze-drying was then heated sequentially: 80 °C for 1 h, 150 °C for 1 h, 200 °C for 30 min, 250 °C for 30 min, and 350 °C for 30 min to obtain the final sample.

2.4 Characterization

The microstructure of the material was characterized by a scanning electron microscopy (SEM) produced by Thermo Apreo C, the

molecular structure of the material was characterized by Fourier transform infrared spectroscopy (FT-IR, iS10), the crystallinity of the material was characterized by X-ray diffraction spectroscopy (XRD), and the elements of the polymer were characterized by a British KRATOS UltraDLD X-ray photoelectron spectrometer.

3 Results and discussion

3.1 Formation and morphology of Ag@PINF

To achieve *in-situ* fiber reinforcement and enhance internal conductivity, a diamine monomer with a disulfide bond, AFD, is used to replace the ODA monomer in the preparation of the polyamicacid spinning solution. The viscosity of the solution is controlled to meet spinning requirements under a nitrogen atmosphere. Polyimide fibers are then fabricated using a high-speed directional spinning process. This method improves the uniformity of the fiber molecules, and under the influence of higher traction and electrostatic forces, the material becomes highly oriented. As a result, the strength and modulus of the fibers are significantly enhanced. Figure 1(a) is a schematic diagram of the preparation of highly oriented spinning.

As shown in Fig. 1(b), the diameter distribution of polyimide fibers produced using the high-speed directional spinning process is more uniform, avoiding the degree of cross-linking typically observed with conventional spinning methods. By incorporating an appropriate amount of S–S dynamic bonds into the polyamic acid solution, the material gains enhanced robustness. Energy spectrum mapping analysis of the prepared directional spun fibers reveals an even distribution of the S element across the fibers. The fibers are then chopped using the high-speed shear force of a homogenizer to produce short-cut PI fibers containing sulfur (Fig. 1(c)). By adding a premixed salt solution of sodium citrate, silver nitrate, and potassium iodide to boiling water containing ascorbic acid and

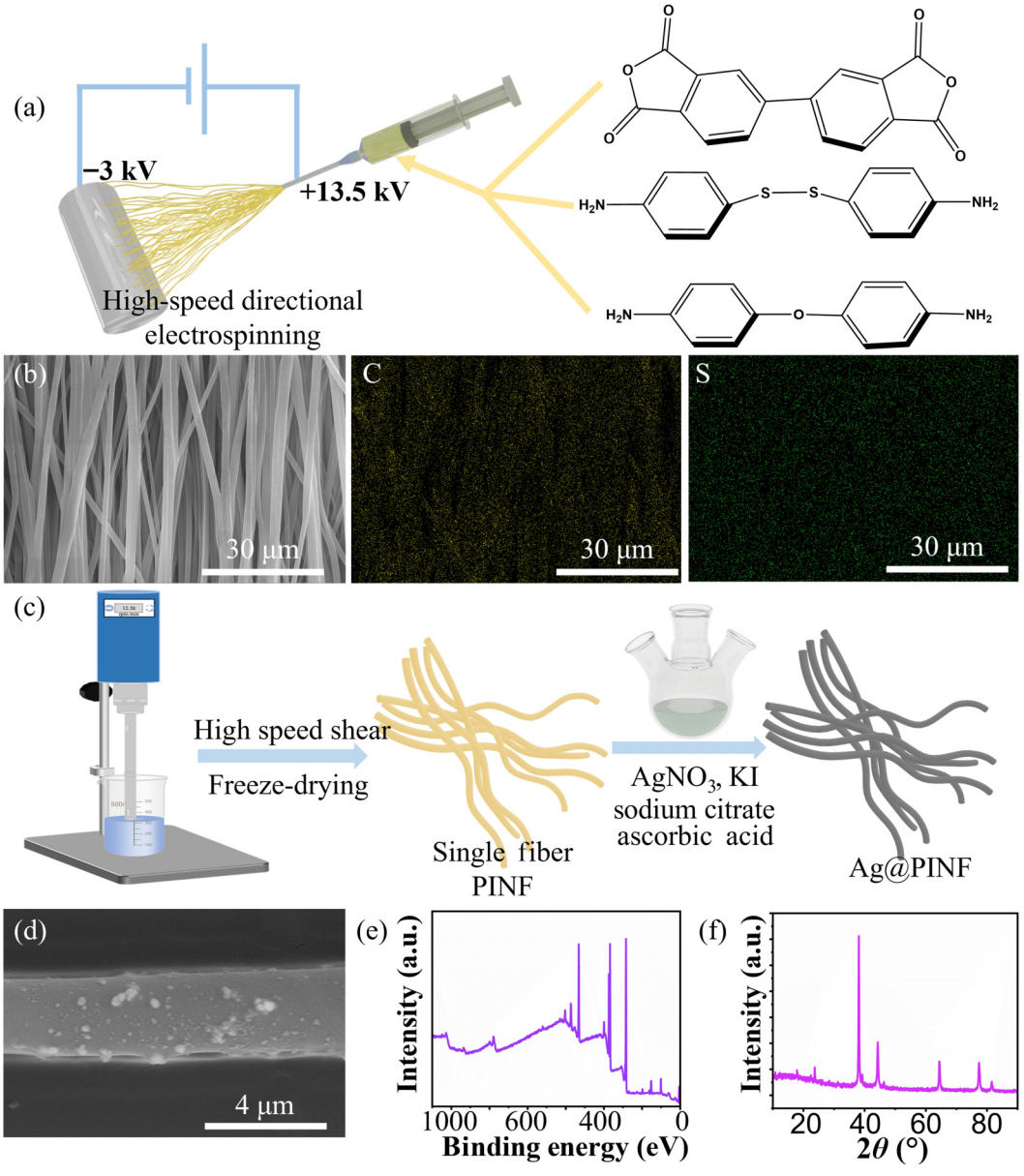

Figure 1 Preparation of Ag@PINF composite materials. (a) Schematic diagram of high-speed directional spinning. (b) SEM and mapping images of PI fiber. (c) Schematic diagram of preparing Ag@PINF. (d) SEM image of Ag@PINF. (e) XPS result of Ag@PINF. (f) XRD result of Ag@PINF.

PINF, Ag nanoparticles are grown *in-situ* on PINF through the synergistic effect of Ag–S bonding. As the solvent is aqueous, the Ag particles are not coated with organic ligands, thereby avoiding limitations in the application of Ag particles within composite materials and imparting a certain level of electronic conductivity to PINF.

The coated chopped fibers were also analyzed using X-ray photoelectron spectroscopy (XPS). The results revealed a distinct binding energy of Ag at 368.1 eV, as shown in Fig. 1(e). Additionally, the composite fibers were further characterized by XRD analysis (Fig. 1(f)). The XRD results indicated a weak amorphous peak for PI at 19°, and characteristic diffraction peaks for Ag at 38°, 45°, 66°, 77°, and 84°, corresponding to the (111), (200), (220), (110), and (112) crystal planes, respectively. SEM, XPS, and XRD characterizations of the composite chopped fibers confirm that short polyimide nanofibers, coated with Ag nanoparticles, have been successfully prepared. Figure 1(d) presents an optical photograph of the coated short-cut single fiber, captured using SEM. The image clearly shows that the Ag nanoparticles, grown *in-situ* using the environmentally friendly aqueous solvent method, are successfully loaded onto the PINF.

3.2 Synthesis of composite conductive aerogel based on fiber *in-situ* reinforcement

Through the fiber reinforcement strategy, we aim to develop composite polyimide aerogels with uniform fiber dispersion and a stable structure. In our previous research, we demonstrated that ultrasound-assisted freeze-drying can be used to prepare CNTs-reinforced polyimide composite aerogels with excellent structural stability and electrical conductivity. Ultrasound-assisted freeze-dispersion technology offers significant advantages in the preparation of composite aerogels. The high-frequency vibrations from ultrasound effectively disperse the components, preventing particle aggregation and ensuring uniformity and consistency in the material. Moreover, this technology allows precise control over pore size distribution and mechanical properties, enhancing the mechanical strength and stability of the composite aerogel. Therefore, ultrasound-assisted freeze-dispersion technology provides an efficient, controllable, and high-performance solution for preparing advanced composite aerogels.

Figure 2(a) presents a schematic diagram illustrating the principle behind the preparation of fiber-reinforced polyimide composite aerogels using ultrasound-assisted freeze-drying. The process begins with the use of ODA and BPDA as the base resin, and TEA is added to convert polyamic acid into a green, environmentally friendly soluble polyamic acid salt. A specific amount of polyamic acid salt and 20 wt.% CNTs are combined in a cylindrical glass container. To reinforce the solution, varying amounts of chopped polyimide fibers are added. The composite materials are labeled according to the fiber-to-PAAs mass ratios: PINF15 (1:5), PINF25 (2:5), PINF35 (3:5), PINF45 (4:5), and PINF55 (5:5). After preparing the composite aerogel precursor solutions, a measured amount is placed in an ultrasonic cleaning machine, where liquid nitrogen is used to cool the ethanol solution to −20 °C. Ultrasonic energy assists the freezing process, promoting the formation of ice crystals while improving the dispersion of components. This process also helps control the direction and size of the ice crystals, optimizing the structure of the composite polyimide aerogel. The composite aerogel is then freeze-dried at −60 °C and 2 Pa in a vacuum for 72 h. Finally, after gradient heating, the polyimide aerogel flexible sensing material is obtained.

The microstructure of the polyimide composite aerogel was examined using a SEM. Figures 2(b)–2(f) display SEM images of PINF15, PINF25, PINF35, PINF45, and PINF55, respectively. The

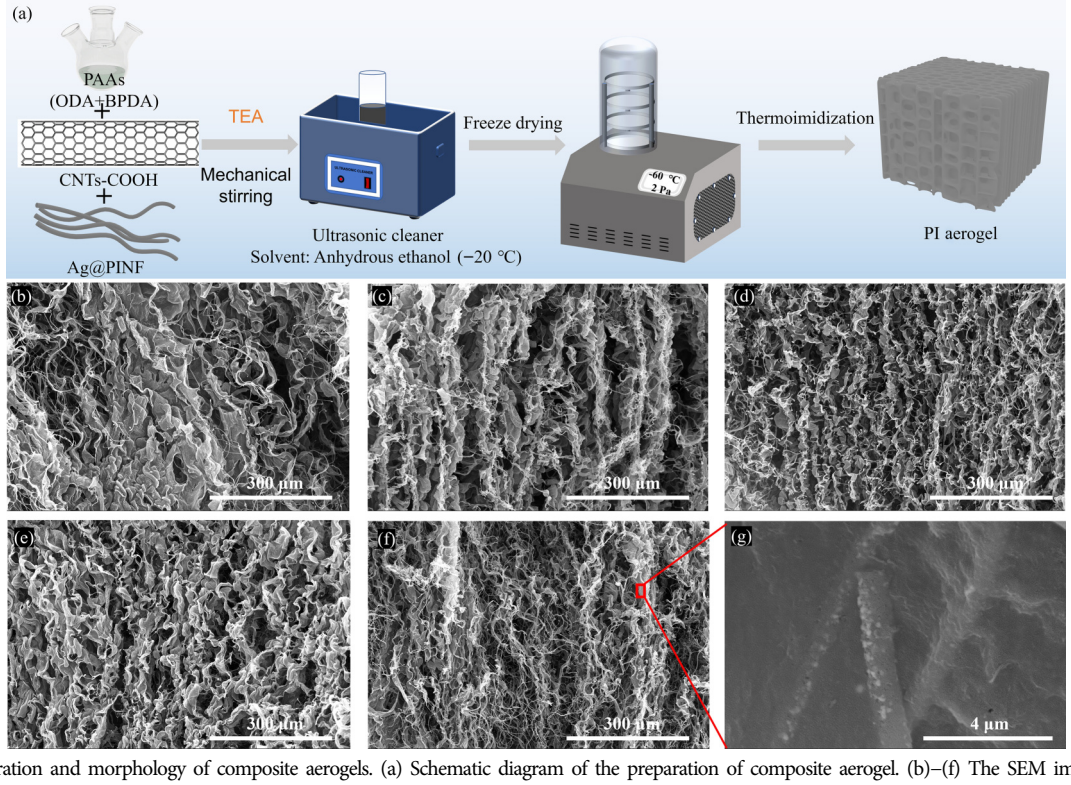

Figure 2 Preparation and morphology of composite aerogels. (a) Schematic diagram of the preparation of composite aerogel. (b)–(f) The SEM images of PINF15, PINF25, PINF35, PINF45, and PINF55. (g) A partial SEM enlarged image of PINF55.

microstructure analysis reveals that all aerogels exhibit well-defined pore structures at the same magnification, with the pore distribution showing a clear evolution as the fiber content increases. At lower fiber concentrations, the aerogel's pore size is highly heterogeneous, featuring both large and small pores. This irregular pore structure negatively impacts the material properties. As the fiber content increases, the fiber distribution within the aerogel matrix becomes more uniform, which regulates the pore formation process. As a result, the pore size distribution becomes more consistent, and the overall pore structure becomes more compact. This trend suggests that the addition of fibers promotes the rearrangement and densification of the matrix material, thereby improving the structural stability and uniformity of the aerogel. Furthermore, with a higher fiber content, the SEM images show a more prominent fiber network on the aerogel surface, indicating the formation of a denser network structure. This enhances the mechanical properties of the aerogel and helps preserve the integrity of its porous structure. The uniform fiber distribution and enhanced surface coverage contribute to the aerogel's improved structural stability and durability, particularly under high-temperature conditions. Therefore, by adjusting the fiber content, the pore structure of the aerogel can be finely tuned, achieving more uniform pore size distribution, structural densification, and a stronger surface fiber network. These changes significantly optimize the overall performance of the aerogel.

Through detailed analysis of the micromorphology, Fig. 2(g) clearly shows that the polyimide fibers are embedded within the aerogel walls, effectively supporting the overall structure of the aerogel. Additionally, the *in-situ* coated Ag nanoparticles are uniformly distributed on the surface of the reinforcing fibers, demonstrating a strong bond between the Ag particles and the polyimide fibers during the coating process. Furthermore, during the subsequent ultrasound-assisted freeze-drying process, the Ag nanoparticles remained securely attached to the fibers, preventing detachment despite the ultrasonic energy. This retention ensures the structural stability of the material, which is crucial for enhancing the conductivity of the aerogels. These results highlight the significant advantages of this process in preparing high-performance conductive composite materials.

First, the molecular structure of the composite aerogel was analyzed using infrared spectroscopy (Fig. 3(a)). As shown in the figure, after annealing, polyamic acid was successfully converted into polyimide, as evidenced by the disappearance of the –OH stretching vibration peak at 3400 cm^{-1}. Additionally, the composite aerogels of all five components displayed asymmetric and symmetric stretching vibration peaks of the C=O group in the polyimide acyl group at 1781 and 1720 cm^{-1}, as well as the C–N stretching vibration peak on the imide ring at 1365 cm^{-1}. Infrared analysis confirmed that the addition of Ag did not affect the transformation of polyamic acid to polyimide. Further XRD spectral analysis of the composite aerogel revealed that the incorporation of composite chopped fibers did not alter the overall crystallization behavior of the material, but the peak intensity gradually increased as the fiber content increased. This is attributed to the addition of Ag@PINF fibers, which, aided by ultrasonic energy, were more evenly dispersed throughout the composite material, providing enhanced structural support to the aerogel matrix. The X-ray diffraction scan also indicated the presence of

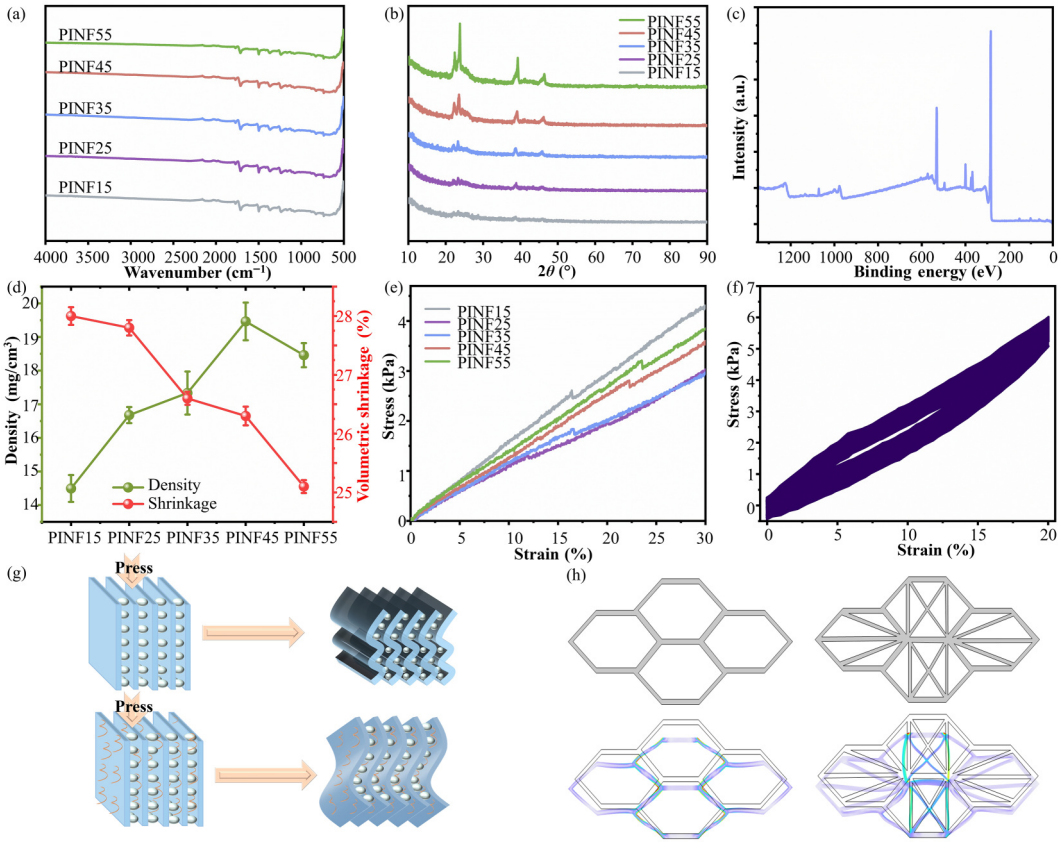

Figure 3 Structure and properties of composite aerogels. (a) FT-IR spectra. (b) XRD results. (c) XPS results. (d) Density and shrinkage. (e) Stress–strain curves. (f) 1000 cycles stress–strain curves. (g) Structural compression diagram. (h) Compressed finite element simulation.

polyimide and CNTs. As the fiber content increased, the silver particle content in the system also increased, exposing more Ag@PINF fibers on the surface of the composite aerogel, which in turn caused the XRD peak intensity to rise gradually (Fig. 3(b)). To further investigate, PINF45 was characterized by XPS full spectrum analysis (Fig. 3(c)), which revealed a distinct Ag binding energy at 368.1 eV, confirming the presence of Ag atoms in the composite aerogel. This finding suggests that the Ag particles provide additional electron conduction sites during the flexible sensing process, thereby improving the material's overall conductivity and enhancing its internal conductive pathways. This, in turn, ensures more stable signal transmission in the aerogel sensing material.

Density is a crucial factor influencing the structure and performance of aerogels. Lower density generally correlates with higher porosity and a finer pore structure, contributing to superior thermal insulation properties and a high specific surface area. However, low-density aerogels may exhibit fragile mechanical strength and structural instability, making them prone to breakage or deformation under external pressure or impact [35]. In contrast, increasing the density of aerogels enhances their mechanical strength and compressive resistance, making them more robust when subjected to larger loads. The use of fiber-reinforced composite aerogels has shown significant advantages in improving mechanical properties. The *in-situ* distribution of fiber networks within the aerogel matrix effectively optimizes the material's microstructure. The introduction of fibers not only disperses stress concentration points, reducing the risk of brittle fracture, but also enhances the compressive and tensile properties of the aerogel without significantly increasing its overall density. Figure 3(d) shows the density distribution of composite aerogels with five different fiber contents. As the content of chopped fibers increases, the overall density trends upward, although the increase is modest. It is important to note that shrinkage during the freeze-drying process can affect aerogels [36]. The shrinkage rate provides an intuitive measure of the stability and uniformity of the aerogel's internal microstructure. Controlling the shrinkage rate is crucial for optimizing the aerogel's density and mechanical properties. By monitoring the shrinkage trend, the pore size distribution and overall density can be precisely adjusted, leading to enhanced mechanical properties. As shown in Fig. 3(d), the volume shrinkage test of the composite aerogels indicates that as the amount of PINF fiber increases, the shrinkage rate decreases. The internal structure of the aerogel becomes progressively more stable with the increase in chopped fibers, limiting shrinkage during the early stages of freeze-drying and the thermal imidization process. This stability provides a favorable foundation for improving the mechanical properties of the composite material.

Mechanical properties are a crucial factor for flexible sensing materials, as they ensure the structural integrity of the material under external pressure and prevent damage due to rupture [37]. Figure 3(e) presents the stress–strain curves of five different composite aerogels subjected to 30% compression. From the curves, it is evident that after fibers are added to reinforce the aerogel structure, the stress–strain curve exhibits a distinct linear relationship. This linear behavior is significant for the application of flexible sensing materials, as it indicates that the material responds to external pressure in a uniform and predictable manner, preventing sudden structural failure or nonlinear deformation. Such stable mechanical behavior helps maintain the continuity and consistency of the conductive network, ensuring that the number of conductive paths remains stable under compression. When compressed, the linear response effectively controls the distance change between conductive particles, preventing instability in signal monitoring caused by excessive proximity or separation of the particles. Specifically, linear compression allows the conductive path to extend or contract uniformly under different strains, ensuring that the number of contact points between conductive particles stays within a reasonable range, thereby enhancing the sensing capability of the composite material. The PINF25 sample was chosen to undergo a thousand-cycle compressive strain test at 20% to assess the durability of the composite aerogel material (Fig. 3(f)). As shown in Fig. 3(f), after one thousand cycles, the stress–strain curve of the composite material remained stable, exhibiting only a slight upward shift, indicating that the composite material possesses excellent durability.

Figure 3(g) illustrates the principle of fiber reinforcement. By comparison, it is evident that after applying pressure to the aerogel sheet without fiber reinforcement, the molecular structure exhibits irregular bending deformation. In contrast, the aerogel sheet reinforced with PINF short fibers shows more uniform deformation under the same pressure. This explains why the stress–strain curve of the fiber-reinforced aerogel exhibits a linear relationship. Additionally, we simulated the force-deformation relationship in the fiber-reinforced structure using finite element analysis. Figure 3(h) presents a schematic model comparing the microstructures with and without fiber reinforcement. When the same pressure is applied, the monomer unit fibers in the fiber-reinforced structure help disperse the force, ensuring uniform distribution within the unit. In contrast, the structure without fiber reinforcement transmits the force to other units, causing the stress–strain curve of the material to exhibit a nonlinear trend. Therefore, *in-situ* short fiber reinforcement during the synthesis process not only addresses the dispersion issue through the principle of "like dissolves like" but also optimizes the mechanical properties of the material. This reinforcement ensures the material's lightness, reduces the inherent shrinkage of aerogels, and improves the structural stability of the composite material.

3.3 Room temperature sensing capability

Ultrasonic dispersion is an efficient method for material handling, particularly in the field of flexible sensing [44]. When used to disperse conductive materials, ultrasonic dispersion plays a crucial role in ensuring the stability and consistency of sensor performance. It evenly distributes conductive materials in the flexible base resin, which significantly improves sensor sensitivity and enables the accurate detection of small changes. Moreover, ultrasonic dispersion helps build a robust conductive network that reduces resistance and enhances the sensor's response speed. During material preparation, the ultrasonic-assisted freeze-drying process facilitates the uniform dispersion of CNTs and Ag@PINF in the polyimide matrix resin. Sensitivity is a key performance indicator for resistive flexible strain sensors. It measures the linear relationship between the sensor's response signal and the applied strain. Figure 4(a) presents the strain response sensitivity (GF), while Fig. 4(b) shows the stress response sensitivity (S). Both sensitivities are expressed in terms of the relative resistance change rate of the composite aerogel ($\Delta R/R_0 = (R_0 - R)/R_0$, where R is the real-time resistance value and R_0 is the initial resistance value). From the trends in both figures, it is evident that the resistance change increases linearly under 25% deformation. This linearity is

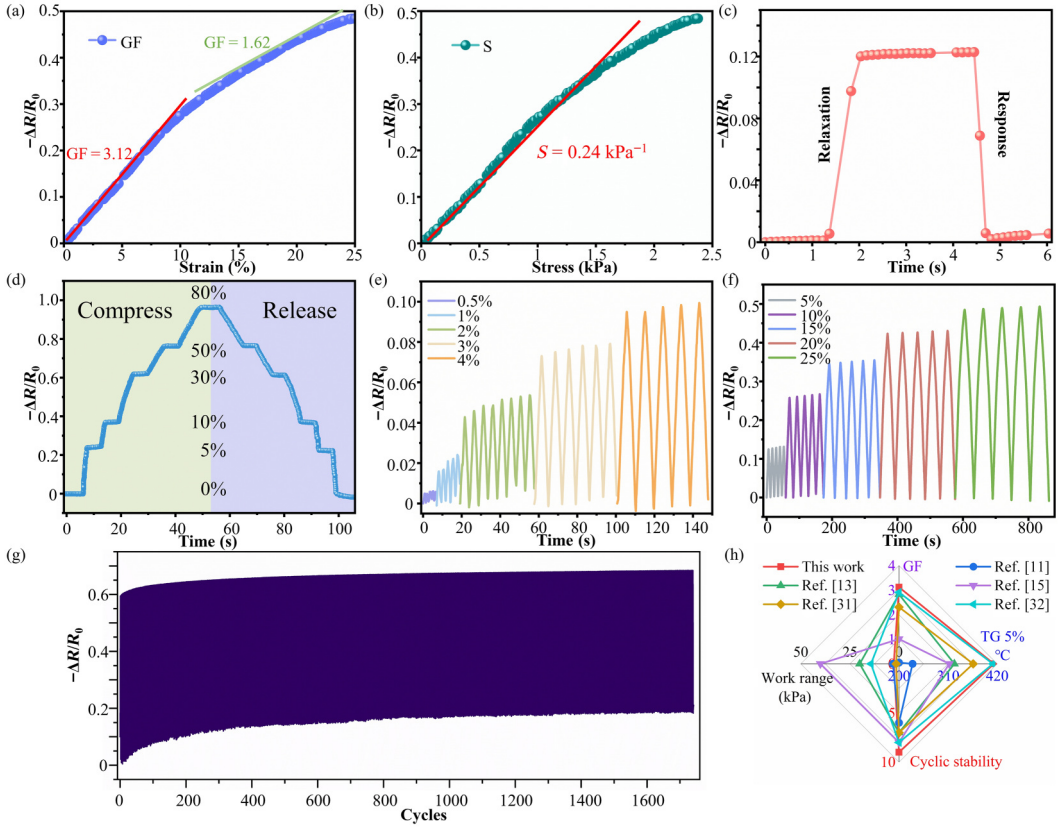

Figure 4 Flexible sensing performance at room temperature. (a) Strain response sensitivity (GF). (b) Pressure response sensitivity (*S*). (c) Response time. (d) Gradient compression response test. (e) Small deformation cyclic response. (f) Mid-stage deformation cycle response. (g) Long-term durability test. (h) Performance comparison radar chart.

attributed to the structural optimization achieved through ultrasonic dispersion. During compressive strain, stress and strain show a linear relationship. The ultrasonic dispersion ensures uniform distribution of conductive particles within the composite material. As strain increases, the resistance change rate also increases linearly, providing a stable and reliable data output for real-time monitoring. The sensor prepared in this study exhibits a GF of 3.12 and an *S* of 0.24 kPa^{-1}.

Additionally, the sensor's response time was measured at a compression speed of 200 mm/min. The composite aerogel material shows a response time of 116 ms and a recovery time of 132 ms (Fig. 4(c)). Figure 4(d) illustrates the strain response stability under different deformations. It is observed that when the stability time is maintained at 5 s under various strains, the resistance signal remains stable, confirming that the prepared sensing material can accurately reflect real-time deformation. Moreover, the composite material maintains good stability during deformation recovery at the same speed. This stability, coupled with the material's structure, ensures reliable performance even after experiencing irreversible deformation.

Through cyclic response testing of the composite material, it was observed that under weak deformation (0.5%), the sensing material responds stably to cyclic changes (Fig. 4(e)). Further cyclic tests revealed that the material demonstrated excellent stability under both low strain (< 5 %) and medium strain (< 25 %) (Fig. 4(f)). To assess the stability of electrical signal transmission, the composite aerogel underwent over 1000 cyclic compression cycles at a constant deformation of 20%. The results, shown in Fig. 4(g), indicate that during long-term cyclic compression, the resistance change rate remains stable, confirming that the prepared composite aerogel sensing material exhibits excellent cyclic stability. Figure 4(h) presents a performance comparison of the flexible piezoresistive strain sensors developed in this study and those reported by other researchers. The results highlight that the composite aerogel material developed here demonstrates distinct advantages in terms of stability, sensitivity, and thermal stability compared to existing materials.

As previously mentioned, the composite aerogel material exhibits excellent conductivity, structural integrity, stability, and durability—properties essential for flexible strain sensors. To demonstrate its potential, human behavior monitoring was conducted by placing the sensor on the throat, finger joints, and knees. Figure 5(a) shows the detection of throat swallowing behavior, Fig. 5(b) depicts finger bending behavior, and Fig. 5(c) illustrates knee bending behavior. The results reveal that the $\Delta R/R_0$ value remains stable, with the sensor returning to a value close to its initial state after each cycle of human motion. These findings indicate that the material offers high sensitivity, stability, and reproducibility. Thus, the composite aerogel material demonstrates significant potential as a wearable flexible sensing device for human motion monitoring.

In flexible piezoresistive strain sensors, the performance is primarily determined by the number of conductive paths, the distance between conductive particles, and the overall conductive properties of the material. To explore the microscopic conductive mechanism in flexible piezoresistive strain sensors, this project

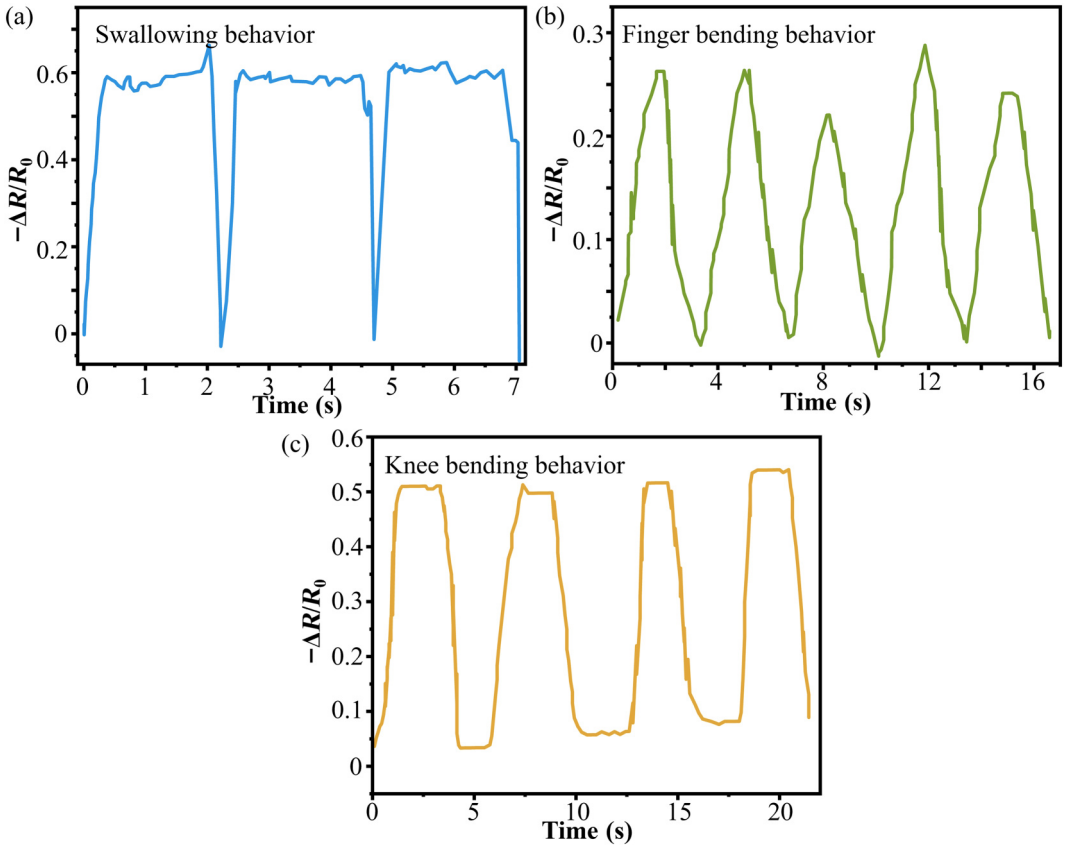

Figure 5 Human motion behavior detection. (a) Throat swallowing, (b) finger bending, and (c) knee bending.

employs computational simulation methods. From a microscopic viewpoint, the resistance change in the composite aerogel is mainly driven by the interaction between the conductive filler and the insulating matrix within the composite material. When external forces are applied, the variation in the distance between conductive particles determines the number of conductive paths, which in turn affects the sensor's stability.

The total resistance R of a polymer composite is generally described by the following equation: $R = R_a + R_b$, where R_a is the resistance between adjacent conductive fillers and R_b is the resistance of the conductive particles themselves [45]. However, in macroscopic materials, R_b can typically be neglected, allowing the composite material's resistance to be approximated by R_a. Here, M and N represent the number of particles required to form a conductive path and the number of conductive paths inside the material, respectively [46]. According to the tunneling model effect, the expression for R_a is given by the following Eq. (4), where h is Planck's constant, c^2 is the effective cross-section, e is the electron charge, s is the average distance between adjacent conductive particles, m_e is the electron mass, and δ is the tunneling barrier height.

According to the experimental results, applying pressure to the composite aerogel reduces the tunneling distance between conductive particles and increases the number of conductive paths.

$$R = M(R_a + R_b)/N \tag{1}$$

$$R_a = \frac{8\pi hs}{3c^2re^2}\exp(vs) \tag{2}$$

$$v = 4\pi\sqrt{2m_e\Delta}/h \tag{3}$$

$$R = \frac{M}{N}\left[\frac{8\pi hs}{3c^2re^2}\exp(vs)\right] \tag{4}$$

Assuming the tunneling distance between adjacent particles changes with the compression deformation x, and the number of conductive networks also changes with strain, these variations follow a specific functional relationship. Let the initial distance between particles be s_0, the distance after compression be s, the initial number of conductive paths be N_0, and the number of conductive paths after compression be N. Based on this, the changing trends of these two variables can be described by the following Eqs. (5) and (6), respectively

$$s = s_0(1 - Ax) \tag{5}$$

$$N = N_0\exp(Bx + Cx^2 + Dx^3 + Ex^4) \tag{6}$$

$$f(x) = Bx + Cx^2 + Dx^3 + Ex^4 \tag{7}$$

$$\frac{\Delta R}{R_0} = \frac{R}{R_0} - 1 = \frac{s}{s_0} \times \frac{N_0}{N}\exp(vs - vs_0) - 1 = (1 - Ax)\exp[v(s - s_0) - f(x)] - 1 \tag{8}$$

$$F = vs_0A + B \tag{9}$$

$$t(x) = v(s - s_0) - f(x) = Cx^2 + Dx^3 + Ex^4 + Fx \tag{10}$$

$$\frac{\Delta R}{R_0} = (1 - Ax)\exp\left[Cx^2 + Dx^3 + Ex^4 + Fx\right] - 1 \quad (11)$$

$$\frac{N}{N_0} = \exp\left[-t(x)\right] \quad (12)$$

In the actual strain process, as the deformation increases, the conductive path inside the sensor also increases. Assuming a 100% compression leads to an infinite number of conductive paths, the final equation derived is Eq. (11), which is expressed as a combination of the resistance change rate and strain. Since the stress–strain curve in the results measured in this experiment closely follows a composite linear change, the constants *C*, *D*, and *E* are all equal to 0. Figure 6 shows the equation fitting of the theoretical calculation and the experimental results. The results indicate that this theoretical model can accurately verify and describe the consistency between the experimental outcomes and the theoretical predictions. According to the fitting results, as compression increases, the distance between conductive particles inside the material decreases, and the number of conductive paths increases rapidly. Using this calculation equation, the distance between the conductive network inside the piezoresistive aerogel sensor and the adjacent particles can be derived. Furthermore, this method can provide new insights for the theoretical calculation of other types of piezoresistive sensors in the future, enabling more in-depth theoretical analysis through parameter fitting techniques.

3.4 High temperature sensing capability

The ability to perform flexible sensing at high temperatures has always been a challenge for traditional flexible strain sensors. However, the polyimide material used in this experiment as a flexible matrix effectively addresses this issue. By placing the intrinsic fiber-reinforced aerogel composite material prepared in this project on a heating platform, the flexible sensing ability of the composite material under high-temperature conditions was tested by setting different platform temperatures and using a circulating compressor. Figure 7(a) shows the cyclic sensing ability test at 50 °C, where the material exhibits good cyclic stability at this temperature. Further cyclic stability tests were conducted at 100 °C (Fig. 7(b)) and 200 °C (Fig. 7(c)). At these higher temperatures, the prepared composite aerogel maintains high cyclic stability. Comparing the relative resistance change rate under the same deformation at the three different cyclic temperatures reveals that as the temperature increases, the detected value remains stable. The increase in electron migration rate due to the temperature rise does not affect the strain behavior detection values, demonstrating that the material can consistently detect strain even at elevated temperatures.

High-temperature testing is not limited to examining changes within a specific temperature range. More importantly, it is essential to assess the stability of detection over long-term high-temperature application. To this end, the prepared composite aerogel flexible sensing material was placed in an oven at 200 °C for 24 h for aging, after which it was cooled to room temperature to test its flexible sensing ability post high-temperature storage. Figure 7(d) shows the strain response time and recovery time after aging. Following the aging process, the response time is 118 ms and the recovery time is 138 ms, which are nearly identical to the response time before aging. This stability is attributed to the good structural integrity of the fiber-reinforced aerogel, which remains relatively intact even after long-term aging. Additionally, the strain response sensitivity (GF) of the composite aerogel was tested. As shown in Fig. 7(e), the

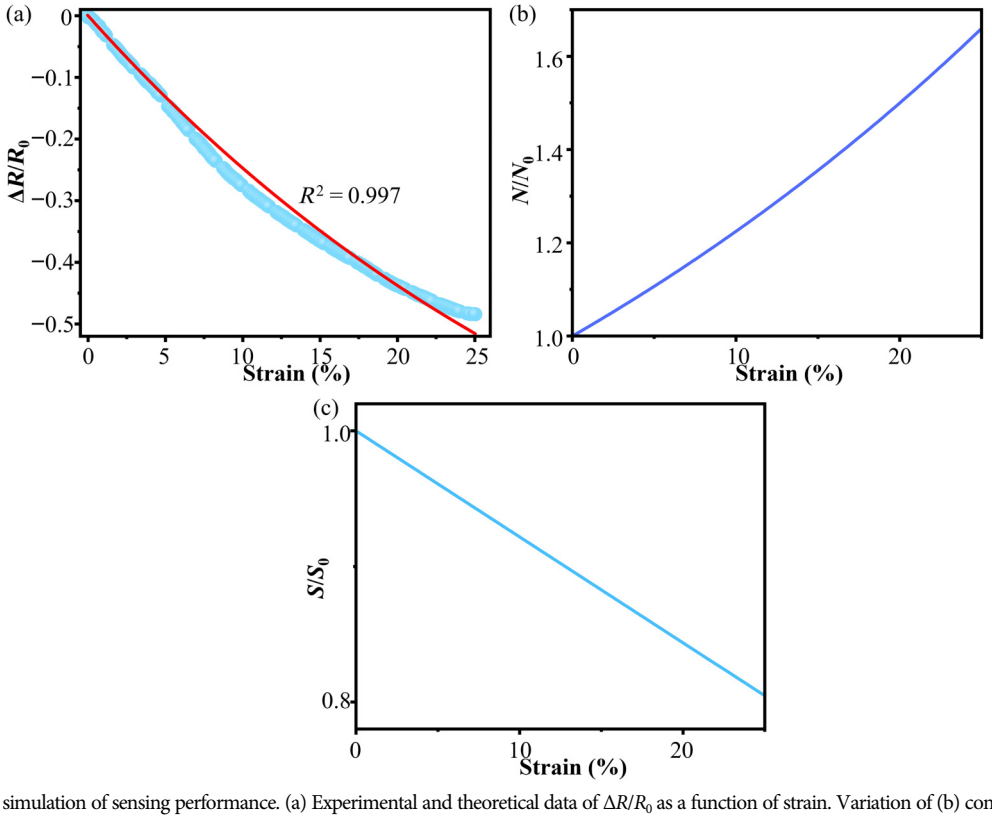

Figure 6 Theoretical simulation of sensing performance. (a) Experimental and theoretical data of $\Delta R/R_0$ as a function of strain. Variation of (b) conductive pathways and (c) adjacent conductive particles of strain sensor.

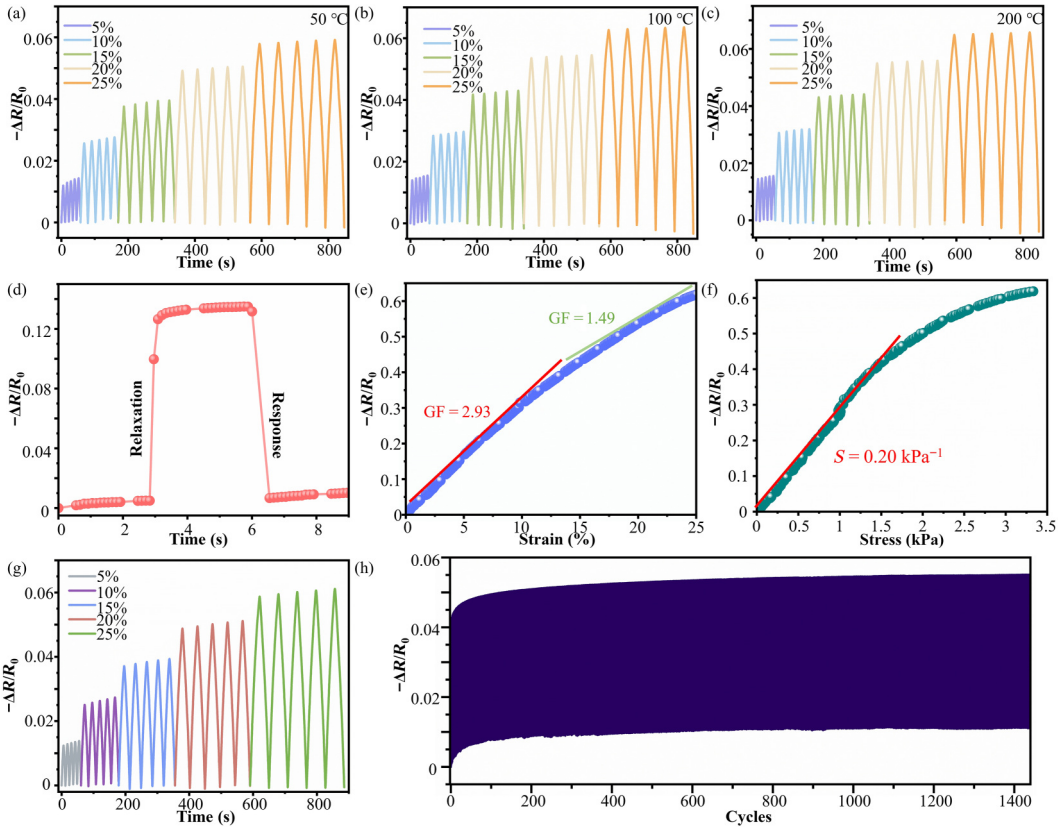

Figure 7 High temperature flexible transmission performance. (a) Cyclic sensing at 50 °C. (b) Cyclic sensing at 100 °C. (c) Cyclic sensing at 200 °C. (d) Response time after aging. (e) Strain sensitivity after aging. (f) Stress sensitivity after aging. (g) Cyclic response after aging. (h) Long-term cycle stability test after aging.

response sensitivity after high-temperature aging demonstrates a slight decrease. This can be attributed to the S–S dynamic bonds in the reinforcing fiber. Under prolonged high-temperature conditions, the fibers fuse further with the aerogel matrix, reducing the number of conductive particles that can move, which in turn decreases the material's sensitivity. Figure 7(f) presents the stress response sensitivity, which also exhibits a downward trend. This is due to the embedding of short-cut fibers into the aerogel wall, which increases the rigidity of the material and results in a reduced response to stress at 25% deformation. Figure 7(g) shows a cyclic compression test of the aged aerogel. Despite aging, the aerogel maintains a stable cyclic response during multiple compression cycles. The results are consistent with pre-aging test data and the cyclic test data at different temperatures, demonstrating that the fiber-reinforced composite aerogel material can deliver consistent sensing data across various temperature environments. This confirms the material's potential for use in flexible sensing applications at high temperatures. Long-term cyclic stability after aging is crucial for verifying the durability of the sensing material. Figure 7(h) shows the long-term cyclic stability test post-aging. The results reveal stable fluctuations even after more than a thousand cycles, indicating that the fiber-reinforced composite aerogel exhibits excellent environmental stability and durability.

4 Conclusions

In summary, we have successfully developed an intrinsic fiber-reinforced flexible composite sensor material. By combining high-speed directional spinning technology with the green *in-situ* growth of silver metal particles, we have optimized an ultrasonic-assisted freeze-drying process to efficiently produce an environmentally friendly polyimide composite aerogel for flexible sensing applications. The fiber-reinforced composite structure enhances the material's structural stability while significantly improving its overall sensing performance. The resulting conductive polyimide composite aerogel exhibits fast response times (116 ms), high sensitivity (GF = 3.12), a low detection limit (0.5% deformation), and excellent long-term cyclic stability (> 1000 cycles). Notably, the strain detection values remain stable under both high-temperature testing and high-temperature aging conditions, demonstrating that the sensor's performance is unaffected by temperature variations. We believe that the intrinsic fiber-reinforced structure offers new possibilities for the development of high-temperature flexible sensing materials.

Data availability

Additional data related to this paper may be requested from the corresponding author upon request.

Acknowledgements

This work is granted by Science Foundation of National Key Laboratory of Science and Technology on Advanced Composites in Special Environments (No. JCKYS2024603C009).

Declaration of competing interest

All the contributing authors report no conflict of interests in this work.

Author contribution statement

J. M. L.: Conceptualization, formal analysis, investigation, writing – original draft. L. W.: Writing – review & editing, funding acquisition. X. R. Z.: Project administration, methodology. X. M. W.: Validation, resources. Z. J. W.: Visualization.

Use of AI statement

None.

References

[1] Yi, Y.; Wang, B.; Liu, X. Y.; Li, C. P. Flexible piezoresistive strain sensor based on CNTs-polymer composites: A brief review. *Carbon Lett.* **2022**, *32*, 713–726.

[2] Wang, S.; Wang, C. Y.; Zhao, Y. F.; Zhang, Y. J.; Zhang, Y. X.; Xu, X. Y.; Lin, Q. J.; Yao, K.; Wang, Y. H.; Han, F. et al. Flexible pressure sensors with ultrahigh stress tolerance enabled by periodic microslits. *Microsyst. Nanoeng.* **2024**, *10*, 24.

[3] Liu, M. S.; Sheng, Y. P.; Huang, C. G.; Zhou, Y. F.; Jiang, L.; Tian, M. W.; Chen, S. J.; Jerrams, S.; Zhou, F. L.; Yu, J. Y. et al. Highly stretchable and sensitive SBS/Gr/CNTs fibers with hierarchical structure for strain sensors. *Compos. Part A Appl. Sci. Manuf.* **2023**, *164*, 107296.

[4] Wang, Y. X.; Yue, Y.; Cheng, F.; Cheng, Y. F.; Ge, B. H.; Liu, N. S.; Gao, Y. H. $Ti_3C_2T_x$ MXene-based flexible piezoresistive physical sensors. *ACS Nano* **2022**, *16*, 1734–1758.

[5] Wu, B. J.; Xie, Z. H.; Shi, Q. W.; Yang, J. L.; Park, C. B.; Gong, P. J.; Li, G. X. Two-dimensional MXene nanosheets on nano-scale fibrils in hierarchical porous structure to achieve ultra-high sensitivity. *Nanoscale* **2024**, *16*, 6961–6972.

[6] Shen, Z. R.; Liu, F. M.; Huang, S.; Wang, H.; Yang, C.; Hang, T.; Tao, J.; Xia, W. H.; Xie, X. Progress of flexible strain sensors for physiological signal monitoring. *Biosens. Bioelectron.* **2022**, *211*, 114298.

[7] Wang, Z. H.; Dong, Y.; Sui, X.; Shao, X. Y.; Li, K. S.; Zhang, H.; Xu, Z. Y.; Zhang, D. Z. An artificial intelligence-assisted microfluidic colorimetric wearable sensor system for monitoring of key tear biomarkers. *npj Flex. Electron.* **2024**, *8*, 35.

[8] Yan, J. F.; Ma, Y. N.; Jia, G.; Zhao, S. R.; Yue, Y.; Cheng, F.; Zhang, C. K.; Cao, M. L.; Xiong, Y. C.; Shen, P. Z. et al. Bionic MXene based hybrid film design for an ultrasensitive piezoresistive pressure sensor. *Chem. Eng. J.* **2022**, *431*, 133458.

[9] Lu, D. X.; Liao, S. Q.; Chu, Y.; Cai, Y. B.; Wei, Q. F.; Chen, K. L.; Wang, Q. Q. Highly durable and fast response fabric strain sensor for movement monitoring under extreme conditions. *Adv. Fiber Mater.* **2023**, *5*, 223–234.

[10] Sheng, T. Y.; He, Q. P.; Cao, Y. D.; Dong, Z. H.; Gai, Y. S.; Zhang, W. Q.; Zhang, D. Y.; Chen, H. W.; Jiang, Y. G. Fish-wearable piezoelectric nanogenerator for dual-modal energy scavenging from fish-tailing. *ACS Appl. Mater. Interfaces* **2023**, *15*, 39570–39577.

[11] Tang, J.; Wu, Y. T.; Ma, S. D.; Yan, T.; Pan, Z. J. Flexible strain sensor based on CNT/TPU composite nanofiber yarn for smart sports bandage. *Compos. Part B Eng.* **2022**, *232*, 109605.

[12] Lin, L. W.; Choi, Y.; Chen, T. Y.; Kim, H.; Lee, K. S.; Kang, J.; Lyu, L.; Gao, J. F.; Piao, Y. Superhydrophobic and wearable TPU based nanofiber strain sensor with outstanding sensitivity for high-quality body motion monitoring. *Chem. Eng. J.* **2021**, *419*, 129513.

[13] Qin, Z.; Chen, X. Y.; Lv, Y. H.; Zhao, B.; Fang, X. H.; Pan, K. Wearable and high-performance piezoresistive sensor based on nanofiber/sodium alginate synergistically enhanced mxene composite aerogel. *Chem. Eng. J.* **2023**, *451*, 138586.

[14] Zhu, S. L.; Lu, Y.; Wang, S. L.; Sun, H. Y.; Yue, Y. Y.; Xu, X. W.; Mei, C. T.; Xiao, H. N.; Fu, Q. L.; Han, J. Q. Interface design of stretchable and environment-tolerant strain sensors with hierarchical nanocellulose-supported graphene nanocomplexes. *Compos. Part A Appl. Sci. Manuf.* **2023**, *164*, 107313.

[15] Cai, J. H.; Li, J.; Chen, X. D.; Wang, M. Nanotube and thermo-expandable microsphere for temperature sensing, microwave shielding and piezoresistive sensor. *Chem. Eng. J.* **2020**, *393*, 124805.

[16] Zhang, H.; Chen, X. Y.; Liu, Y.; Yang, C. Q.; Liu, W. Z.; Qi, M. Y.; Zhang, D. Z. PDMS film-based flexible pressure sensor array with surface protruding structure for human motion detection and wrist posture recognition. *ACS Appl. Mater. Interfaces* **2024**, *16*, 2554–2563.

[17] Yang, C. Q.; Zhang, D. Z.; Wang, D. Y.; Luan, H. X.; Chen, X. Y.; Yan, W. Y. *In situ* polymerized MXene/polypyrrole/hydroxyethyl cellulose-based flexible strain sensor enabled by machine learning for handwriting recognition. *ACS Appl. Mater. Interfaces* **2023**, *15*, 5811–5821.

[18] Yang, C. Q.; Zhang, D. Z.; Wang, W. W.; Zhang, H.; Zhou, L. N. Multi-functional MXene/helical multi-walled carbon nanotubes flexible sensor for tire pressure detection and speech recognition enabled by machine learning. *Chem. Eng. J.* **2025**, *505*, 159157.

[19] Dong, Y.; An, W. Z.; Wang, Z. H.; Zhang, D. Z. An artificial intelligence-assisted flexible and wearable mechanoluminescent strain sensor system. *Nano-Micro Lett.* **2025**, *17*, 62.

[20] Zhang, Z. X.; Xie, C.; Zhang, J. N.; Chan, M.; Zhang, M. Tunable stretchable strain sensors enabled by patterned ecoflex-vertical aligned carbon nanotube arrays and pre-stretching transfer. *Carbon* **2022**, *197*, 218–225.

[21] Hang, T. Y.; Zhou, L. J.; Xu, C. H.; Chen, Y. M.; Shen, J. H.; Zheng, J. J.; Yang, P. G.; Li, X. P.; Luo, H.; Tong, G. X. High-performance wearable bimetallic nanowire-assisted composite foams for efficient electromagnetic interference shielding, infrared stealth, and piezoresistive sensing. *Nano Res.* **2024**, *17*, 6757–6765.

[22] Chen, Y. M.; He, W. W.; Zhou, H. L.; Shen, J. H.; Li, X. P.; Zheng, J. J.; Wu, Z. Y. Compressible and conductive multi-scale composite aerogel elastomers for electromagnetic wave absorption, energy harvesting, and piezoresistive sensing. *Nano Energy* **2024**, *119*, 109100.

[23] Hang, T. Y.; Chen, Y. M.; Yin, F. Q.; Shen, J. H.; Li, X. P.; Li, Z. C.; Zheng, J. J. Highly stretchable polyvinyl alcohol composite conductive hydrogel sensors reinforced by cellulose nanofibrils and liquid metal for information transmission. *Int. J. Biol. Macromol.* **2024**, *258*, 128855.

[24] Fu, R.; Zhao, X.; Zhang, X. Y.; Su, Z. Q. Design strategies and applications of wearable piezoresistive strain sensors with dimensionality-based conductive network structures. *Chem. Eng. J.* **2023**, *454*, 140467.

[25] Gong, T.; Jia, J.; Sun, X. R.; Li, W. D.; Ke, K.; Bao, R. Y.; Yang, W. Design strategy for hierarchical structure of carbon black on microporous elastomer surface toward stretchable and compressive strain sensors. *Carbon* **2023**, *206*, 53–61.

[26] Zeng, Z. H.; Wu, N.; Wei, J. J.; Yang, Y. F.; Wu, T. T.; Li, B.; Hauser, S. B.; Yang, W. D.; Liu, J. R.; Zhao, S. Y. Porous and ultra-flexible crosslinked MXene/polyimide composites for multifunctional electromagnetic interference shielding. *Nano-Micro Lett.* **2022**, *14*, 59.

[27] Yang, X.; Yi, J. Q.; Wang, T.; Feng, Y. N.; Wang, J. W.; Yu, J.; Zhang, F. L.; Jiang, Z.; Lv, Z. S.; Li, H. C. et al. Wet-adhesive on-skin sensors based on metal-organic frameworks for wireless monitoring of metabolites in sweat. *Adv. Mater.* **2022**, *34*, 2201768.

[28] Li, M. L.; Wang, T.; Han, C. D.; Yang, H.; Huang, Y.; Hu, J. H.; Li, L.; Jiang, J.; Huang, M. H.; Fan, Y. et al. A novel piezoresistive sensor with rectification properties. *Mater. Des.* **2024**, *239*, 112782.

[29] Su, Q.; Zou, Q.; Li, Y.; Chen, Y. Z.; Teng, S. Y.; Kelleher, J. T.; Nith, R.; Cheng, P.; Li, N.; Liu, W. et al. A stretchable and strain-

unperturbed pressure sensor for motion interference-free tactile monitoring on skins. *Sci. Adv.* **2021**, *7*, eabi4563.

[30] Yang, W. K.; Liu, S.; Wang, Y. L.; Liu, H.; Liu, C. T.; Shen, C. Y. Advances in multifunctional flexible MXene-based stress sensors. *J. Mater. Chem. C* **2024**, *12*, 7845–7861.

[31] Pu, L.; Liu, Y. P.; Li, L.; Zhang, C.; Ma, P. M.; Dong, W. F.; Huang, Y. P.; Liu, T. X. Polyimide nanofiber-reinforced $Ti_3C_2T_x$ aerogel with "lamella-pillar" microporosity for high-performance piezoresistive strain sensing and electromagnetic wave absorption. *ACS Appl. Mater. Interfaces* **2021**, *13*, 47134–47146.

[32] Liu, J. M.; Weng, L.; Zhang, X. R.; Wu, Z. J. Ultrasonic-assisted freeze-drying for polyimide/carboxylated MWCNTs aerogel sensor with excellent aging sensing performance. *Adv. Mater. Technol.* **2023**, *8*, 2301057.

[33] Sun, J. C.; Zhuo, S. J.; Zhang, R. B. Highly transparent, temperature-resistant, and flexible polyimide aerogels for solar energy collection. *ACS Appl. Mater. Interfaces* **2023**, *15*, 37957–37965.

[34] Sun, Y. L.; Wang, Z. P.; Zhao, J. Y.; Nie, H. R.; Zhou, G. Y. Low shrinkage polyimide aerogels with excellent thermal insulation: Boosted by "paddle-shaped" benzhydrylidenefluorene-based diamines. *Chem. Eng. J.* **2024**, *479*, 147642.

[35] Chen, Z. L.; Chen, J.; Hou, X. B.; Chen, L. M. Mechanically robust and thermal-insulated polyimide aerogel films by polymerization-regulated strategy for flexible thermal protection. *Chem. Eng. J.* **2024**, *496*, 154251.

[36] Tafreshi, O. A.; Saadatnia, Z.; Ghaffari-Mosanenzadeh, S.; Rastegardoost, M. M.; Zhang, C. X.; Park, C. B.; Naguib, H. E. Polyimide aerogel fiber bundles for extreme thermal management systems in aerospace applications. *ACS Appl. Mater. Interfaces* **2024**, *16*, 54597–54609.

[37] Zhang, C.; Wu, M. X.; Cao, S. Y.; Liu, M. J.; Guo, D.; Kang, Z.; Li, M.; Ye, D.; Yang, Z. Q.; Wang, X. W. et al. Bioinspired environment-adaptable and ultrasensitive multifunctional electronic skin for human healthcare and robotic sensations. *Small* **2023**, *19*, 2304004.

[38] Xu, X.; Yan, B. Bioinspired luminescent HOF-based foam as ultrafast and ultrasensitive pressure and acoustic bimodal sensor for human-machine interactive object and information recognition. *Adv. Mater.* **2023**, *35*, 2303410.

[39] Wang, J. W.; Zheng, Y. P.; Cui, T. Y.; Huang, T. Y.; Liu, H. D.; Zhu, J. X.; Song, L.; Hu, Y. Bioinspired ultra-robust ionogels constructed with soft-rigid confinement space for multimodal monitoring electronics. *Adv. Funct. Mater.* **2024**, *34*, 2312383.

[40] Dong, X. D.; Wan, B. Q.; Zheng, M. S.; Yang, X.; Zhang, H. K.; Zhao, Q. L.; Zha, J. W. Versatile spider-web-like cross-linked polyimide aerogel with tunable dielectric permittivity for highly sensitive flexible sensors. *Chem. Eng. J.* **2023**, *465*, 143034.

[41] Xue, T. T.; Yu, Y.; Fu, Z. P.; Wang, Q. Y.; Hu, Z. Y.; Fan, W.; Liu, T. X. Double-network polyimide/silica aerogel fiber for thermal insulation under extremely hot and humid environment. *Compos. Sci. Technol.* **2023**, *242*, 110196.

[42] Liu, C.; Wang, M. K.; Wang, J.; Xu, G. Y.; Zhang, S. Z.; Ding, F. Double-phase-networking polyimide hybrid aerogel with exceptional dimensional stability for superior thermal protection system. *Small* **2024**, *20*, 2404104.

[43] Shi, X. R.; Zhang, K. Y.; Chen, J. X.; Qian, H. Q.; Huang, Y. D.; Jiang, B. Octopi tentacles-inspired architecture enables self-healing conductive rapid-photo-responsive materials for soft multifunctional actuators. *Adv. Funct. Mater.* **2024**, *34*, 2311567.

[44] Xu, L. L.; Chen, H.; Zheng, P. Y.; Zheng, H. W.; Chen, Z.; Liu, Z. L.; Li, P. Y.; Zhao, X.; Peng, Q. Y.; He, X. D. Lightweight and mechanically robust MXene/polyimide/silver nanowire composite aerogels for flexible piezoresistive sensors. *ACS Appl. Nano Mater.* **2023**, *6*, 19098–19107.

[45] Yu, X.; Wu, Z. J.; Weng, L.; Jiang, D. W.; Algadi, H.; Qin, Z. F.; Guo, Z. H.; Xu, B. B. Flexible strain sensor enabled by carbon nanotubes-decorated electrospun TPU membrane for human motion monitoring. *Adv. Materials Interfaces* **2023**, *10*, 2202292.

[46] Wang, X.; Liu, X. H.; Schubert, D. W. Highly sensitive ultrathin flexible thermoplastic polyurethane/carbon black fibrous film strain sensor with adjustable scaffold networks. *Nano-Micro Lett.* **2021**, *13*, 64.